Effects of Sr-site deficiency on structure and electrochemical performance in Sr_2MgMoO_6 for solid-oxide fuel cell

Long Jiang [a, b], Gan Liang [c], Jiantao Han [b], Yunhui Huang [b, *]

[a] School of Physics and Optoelectronic Engineering, Yangtze University, Jingzhou, Hubei 434023, China
[b] State Key Laboratory of Material Processing and Die and Mould Technology, School of Materials Science and Engineering, Huazhong University of Science and Technology, Wuhan, Hubei 430074, China
[c] Department of Physics, Sam Houston State University, Huntsville, TX 77341, United States

HIGHLIGHTS

- The effects of Sr-deficiency in $Sr_{2-x}MgMoO_{6-\delta}$ anodes were investigated.
- Sr-deficiency increases B-site ordering and Mo^{6+} content.
- Single cells with all-perovskite electrodes were fabricated and tested.
- The $x = 0.10$ sample shows the best electrochemical performance.

ARTICLE INFO

ABSTRACT

Double-perovskite Sr-deficient $Sr_{2-x}MgMoO_{6-\delta}$ ($x = 0-0.15$) samples were prepared via a sol—gel route and evaluated as anode materials for solid-oxide fuel cells. The effects of Sr-site deficiency on lattice structure, electrical conductivity, thermal expansion coefficient (TEC) and electrochemical performance were systematically investigated. It is found that Sr-site deficiency within $0 < x < 0.10$ increases the degree of B-site ordering but decreases the TEC value. The electrical conductivity increases with increasing x and reaches the maximum at $x = 0.10$. The Sr-site deficiency also increases the ratio of Mo^{6+}, leading to enhanced oxygen vacancy concentration and reduced polarization resistance. With $La_{0.8}Sr_{0.2}Ga_{0.83}Mg_{0.17}O_{3-\delta}$ as electrolyte and $Ba_{0.5}Sr_{0.5}Co_{0.8}Fe_{0.2}O_{3-\delta}$ as cathode, the single cells with $Sr_{2-x}MgMoO_{6-\delta}$ ($x = 0, 0.05, 0.10$ and 0.15) anodes show the maximum power densities of 527, 551, 659 and 573 mW cm^{-2}, respectively, in H_2 at 800 °C. The $x = 0.10$ anode exhibits the highest power density due to its high conductivity, low overpotential and good catalytic activity. Single-cell tests indicate the potential application of the deficiency in Sr-site for $Sr_{2-x}MgMoO_{6-\delta}$ as SOFC anode material.

© 2014 Elsevier B.V. All rights reserved.

1. Introduction

Solid-oxide fuel cells (SOFCs) are attractive electrochemical devices to convert the chemical energy of fuels directly to electrical energy [1]. Although SOFCs operate at high temperatures, they show some distinctive advantages such as high efficiency, low emission, etc. For SOFCs, anode materials are crucial to achieve high performance since they directly face the fuels. In general, conventional NiO—YSZ and NiO—SDC anode materials exhibit excellent catalytic activity for fuel oxidation and good current collection, but do have some disadvantages, such as low tolerance to sulfur, carbon

deposition in hydrocarbon fuels, and poor redox cycling that causes volume instability [2—4].

Currently the researchers have paid much attention to the mixed ion-electron conductive (MIEC) anode materials that can operate at low temperature, show high catalytic activity in hydrocarbon fuels, and tolerance carbon deposition and sulfur poisoning. For example, Tao et al. reported that $La_{0.75}Sr_{0.25}Cr_{0.5}Mn_{0.5}O_3$ perovskite oxide exhibited high power density by using perovskite as electrolyte [5]. Gorte et al. showed that the electrochemical performance of $SrTiO_3$-based oxides could be remarkably improved using impregnation and infiltration technology [6,7]. Ceria-based ceramic anodes with addition of small amounts of metal Cu could perform reliably in hydrocarbon fuels [8]. However, the power densities of such MIEC anodes are still lower as compared with the

* Corresponding author. Tel.: +86 27 87558241.
E-mail address: huangyh@mail.hust.edu.cn (Y. Huang).

Ni-based anodes due to insufficient conductivity and low surface activity [9,10].

The double-perovskite Sr_2MgMoO_6 (SMMO) is a promising MIEC anode material for SOFCs, which shows high power density in both H_2 and CH_4 fuels, and excellent tolerance to sulfur [11,12]. Based on this double perovskite, a series of A_2MMoO_6 (A = Ca, Sr, Ba; M = Mn, Fe, Co, Ni, Zn) have been investigated [13–17]. The researches indicate that these double perovskites also show good performances as anode materials for SOFCs. However, considering comprehensive properties, Sr_2MgMoO_6 is still the best one due to high power density, stable redox activity and good resistance against carbon deposition and sulfur poisoning [11]. Here, oxygen vacancy plays an important role in carrying oxygen ions during the electrochemical reaction. Thus the presence of oxygen vacancies in the anode materials in reducing atmosphere not only provides high oxide-ion conduction, but also yields the Mo(V)/Mo(VI) redox couple to enhance the electronic conductivity and catalytic activity for fuel oxidation [12].

Much effort has been concentrated on optimizing SMMO to improve electronic or ionic conductivity and catalytic activity. Doping at Sr-site by La^{3+} and Sm^{3+} ions can improve the electro-catalytic activity for fuel oxidation and electrochemical performance [18,19]. Partial substitution of Mg^{2+} by Mn^{2+} or Al^{3+} can increase the electrical conductivity [11,20]. Doping at Mo-site with W and Nb decreases the electrical conductivity, but doping with a small amount of Nb increases the ionic conductivity [21]. These findings demonstrate that doping at Sr-site and Mo-site is an efficient way to modify the electrochemical performance for SMMO. On the other hand, creating cationic deficiency in the lattice of SMMO may cause the change in Mo valence and oxygen vacancy, which should result in modification in catalytic activity and oxide-ion conduction. Hitherto, no report has focused on the effect of Sr-site deficiency in SMMO. In this regard, investigation on how the deviation of Sr-stoichiometry and the resultant Mo-valence affect the properties of SMMO is interesting for us to understand much more features of the double-perovskite anode materials.

In this work, we designed and prepared series Sr-site deficient $Sr_{2-x}MgMoO_{6-\delta}$ (x = 0, 0.05, 0.10, 0.15) materials. For evaluation, single cells were fabricated with $Sr_{2-x}MgMoO_{6-\delta}$ as anode, $Ba_{0.5}Sr_{0.5}Co_{0.8}Fe_{0.2}O_{3-\delta}$ (BSCF) as cathode and $La_{0.8}Sr_{0.2}Ga_{0.83}Mg_{0.17}O_{3-\delta}$ (LSGM) as electrolyte. The effects of Sr-site deficiency on structure, electrical conductivity, thermal expansion and electrochemical performance were systematically investigated.

2. Experiment

$Sr_{2-x}MgMoO_{6-\delta}$ (x = 0, 0.05, 0.10, 0.15) samples were prepared by a sol–gel technique with ethylenediaminetetraacetic acid (EDTA) as chelating agent and $Sr(NO_3)_2$, $Mg(NO_3)_2 \cdot 6H_2O$, and $(NH_4)_6Mo_7O_{24} \cdot 4H_2O$ as cationic precursors. Stoichiometric cationic precursors were dissolved in deionized water, while EDTA was separately dissolved in aqueous ammonia solution. The molar ratio of EDTA to the total of metal ions was 1:1. The above two solutions were mixed together at room temperature under stirring to achieve a clear solution. The pH value of the solution was adjusted to approximately 7 ~ 8 with aqueous ammonia. The obtained solution was stirred at 90 °C on a heating plate till a gel was formed. The gel was kept in an oven at 150 °C overnight till it was completely dried. A black powder was attained after being decomposed at 400 °C in air for 10 h. The powder was then ground and calcined at 800 °C for 8 h in air to burn out the organic species. The resulting powder was reground and pressed into pellets. The pellets were reduced at 1100 °C for 40 h in a flowing atmosphere of 5% H_2/Ar. After cooling down to room temperature, the pellets were reground, repressed,

and finally sintered at 1200 °C for 48 h in 5% H_2/Ar. The electrolyte LSGM and interlayer $Sm_{0.2}Ce_{0.8}O_{2-\delta}$ (SDC) were prepared via solid state reaction, as described in our previous work [22]. The perovskite BSCF cathode material was synthesized via a sol–gel route [23].

Single cells were fabricated by electrolyte-support technique with 280 μm thick LSGM disk as electrolyte. The cell configuration was $Sr_{2-x}MgMoO_{6-\delta}$|SDC|LSGM|BSCF. Firstly, the interlayer SDC was uniformly screen-printed onto one side of the LSGM disk followed by firing at 1300 °C for 1 h in air. The anode ($Sr_{2-x}MgMoO_{6-\delta}$) ink was subsequently printed onto the interlayer and fired at 1250 °C for 2 h in air. The BSCF ink was then painted onto the other side of LSGM disk as cathode and sintered 950 °C for 2 h. Reference electrodes made of the same materials of working electrodes were used to monitor the overpotentials of the anode and cathode [12]. The single cell configuration is shown in Fig. 1. The working electrode area of the cell is 0.16 cm^2 (0.4 cm × 0.4 cm), and the reference electrode area is 0.08 cm^2 (0.4 cm × 0.2 cm). In order to avoid potential gradient along the electrolyte surface, the reference electrode is placed 2.4 mm away (the distance d in Fig. 1a) from the working electrode, which is greater than eight times of electrolyte thickness. We used Ag paste as current collector at both the anode and cathode sides. Considering the possible effect of Ag paste, all the cells were fabricated under the identical conditions.

The phase of the samples was characterized with X-ray diffraction (XRD) by using the Philips X'Pert PRO diffractometer operating with Cu Ka radiation. Rietveld refinement was carried out to determine the structure by using the RIETAN-2000 software. Scanning electron microscope (SEM) was used to observe the morphology of the samples. Surface analysis was performed on an X-ray photoelectron spectrometer (XPS, MULT1LAB2000, VG). The Mo L_3-edge X-ray absorption spectroscopy (XAS) measurements
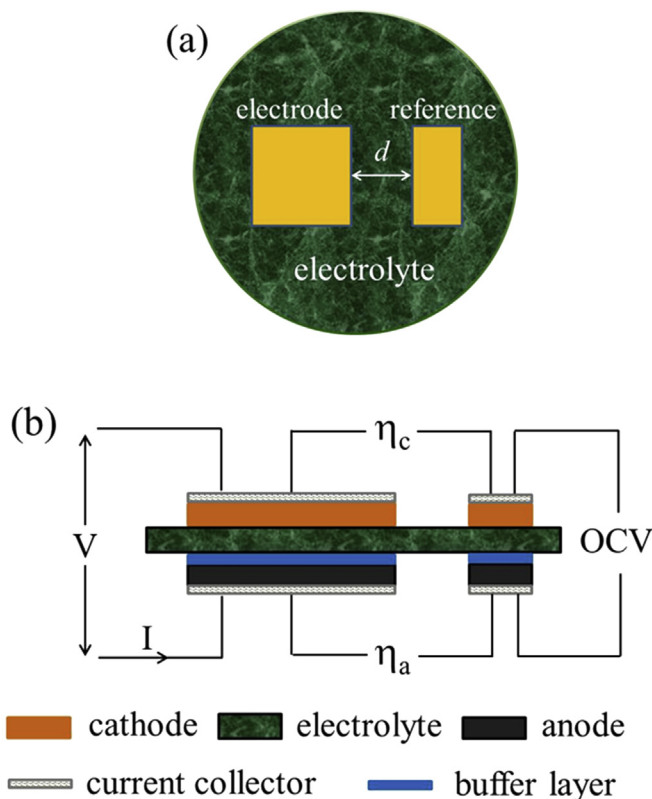

Fig. 1. (a) Top view of the reference-electrode structure for overpotentials, and (b) schematic diagram of the fuel cell test.

were performed in the fluorescence mode and on powdered samples on beamline X-19A at the National Synchrotron Light Source, Brookhaven National Laboratory. The electrical conductivity was measured on an RTS-8 digital instrument under flowing H_2 (50 ml min^{-1}) with a standard four-probe method. For the conductivity measurement, the sample was pressed into a pellet with diameter of 13 mm and thickness of 1 mm under a pressure of 100 MPa followed by sintering at 800 °C for 20 h under 5% H_2/Ar atmosphere. Thermal expansion coefficients (TECs) were measured on the rectangular-shaped bar samples (5 mm × 5 mm × 20 mm) from room temperature to 900 °C at a heating rate of 5 °C min^{-1} by using a dilatometer (NETZSCH STA449c/3/G). Thermogravimetric (TG) behaviors were checked by a Stanton STA 781 instrument. The measurements of TEC and TG were carried out at 5% H_2/Ar atmosphere. Single cells were tested in the vertical furnace with dry H_2 as fuel and ambient air as oxidant. Electrochemical impedance spectra (EIS) and anodic overpotential of single cells were collected by an electrochemical working station (PARSTAT2273, Princeton Applied Research, US).

3. Results and discussion

Fig. 2a displays the XRD patterns of the $Sr_{2-x}MgMoO_{6-\delta}$ ($x = 0$–0.15) samples reduced in 5% H_2/Ar atmosphere at 1200 °C for 48 h. All samples are indexed as double-perovskite phase; only a

weak impurity peak appears at $2\theta = 27.9°$, which is caused by $SrMoO_4$. The A-site deficient $Sr_{2-x}MgMoO_{6-\delta}$ samples shows almost the same diffractions as stoichiometric Sr_2MgMoO_6, indicating that they are structurally stable after being reduced. The stability in double-perovskite structure is mainly determined by the octahedral [BO_6]. We calculated the Goldschmidt tolerance factor, $t = (r_A + r_O)/\sqrt{2}(r_B + r_O)$, from the effective ionic radii of r_A, r_B and r_O to access the structure stability. If $t = 1$, the compound reaches an ideal perovskite structure. The calculated t values are 0.984, 0.971, 0.959 and 0.946 for $x = 0$, 0.05, 0.10 and 0.15, respectively. These values approach 1, indicating the crystal structure of $Sr_{2-x}MgMoO_{6-\delta}$ at reduction atmosphere with Sr-site deficiency range from 0 to 0.15 is stable.

The XRD patterns were analyzed by Rietveld method using triclinic structure with $I\bar{1}$ space group. The profile R_p and weighted profile R_{wp} parameters indicate that the refined results are reliable and acceptable. The lattice parameters, atom occupancy (g_M) and degree of cationic ordering (ξ) obtained by Rietveld refinement are displayed in Table 1. As x increases, the ξ (= $2(g_M -0.5)$) increases and reaches the maximum ($\xi = 0.989$) for $x = 0.10$, and then decreases, which means that the Sr-site deficiency to some extent increases the degree of B-site cationic ordering. For double perovskite $Sr_{2-x}MgMoO_{6-\delta}$, the lattice volume is predicted to decrease with increasing Sr deficiency. However, from the refined result, we find that the lattice volume has the same variation trend as ξ. This could be interpreted that, the coordination number for Mg adapts to match six-coordination of Mo(VI), and the charge imbalance resulted from Sr-site deficiency is compensated by reduction of Mo ions and formation of oxygen vacancies for $x = 0$–0.10; if Sr-deficiency is higher than the limited range, for example $x = 0.15$, the charge compensation balance is carried out by removal of oxygen anion, leading to the increase of Mo(V) proportion. Therefore, the lattice volume first increases and then decreases.

In order to evaluate the surface properties of $Sr_{2-x}MgMoO_{6-\delta}$ ($x = 0$–0.15) and the chemical environment of composite elements, XPS was analyzed by curve-fitting of the O 1s and Mo 3d spectra since the valence states of Sr and Mg ions are stable. The surface chemical composition was investigated by XPS and the results are summarized in Table 2. In Fig. 3a, the O 1s core-level spectra consist of two components at around 529.8 and 531.2 eV. The former is due to the typical hydroxyl groups and carbonate structures (O_H) and the latter corresponds to the lattice O^{2-} (O_L) [14,24]. With deviation of stoichiometry, the ratio of O_L/O_H first increases, reaches the maximum at $x = 0.10$, and then decreases, indicating that the Sr-site deficiency leads to the decrease in the amount of surface carbonate. The surface characteristic of the anode material is important for the electro-catalytic and the transport properties [25]. Increased lattice oxygen in the lattice readily leads to the formation of oxygen

Table 1
Room-temperature lattice parameters, atom occupancy (g_M) and degree of cationic ordering (ξ) obtained by Rietveld Refinement on XRD patterns for $Sr_{2-x}MgMoO_{6-\delta}$ ($x = 0$–0.15).

x value	0	0.05	0.10	0.15
Space group	$I\bar{1}$	$I\bar{1}$	$I\bar{1}$	$I\bar{1}$
a (Å)	5.569(9)	5.568(4)	5.567(5)	5.564(3)
b (Å)	5.569(0)	5.574(5)	5.576(2)	5.575(6)
c (Å)	7.921(4)	7.921(8)	7.922(1)	7.918(0)
α (deg)	90.113	90.100	90.077	89.986
β (deg)	89.939	89.910	89.835	89.834
γ (deg)	90.049	90.076	90.052	90.047
V (Å^3)	245.716	245.908	245.946	245.652
g_M	0.9580	0.9828	0.9945	0.9354
ξ	0.9160	0.9656	0.9890	0.8708
R_{wp} (%)	11.35	8.05	9.94	12.10
R_p (%)	7.63	5.88	6.80	8.57

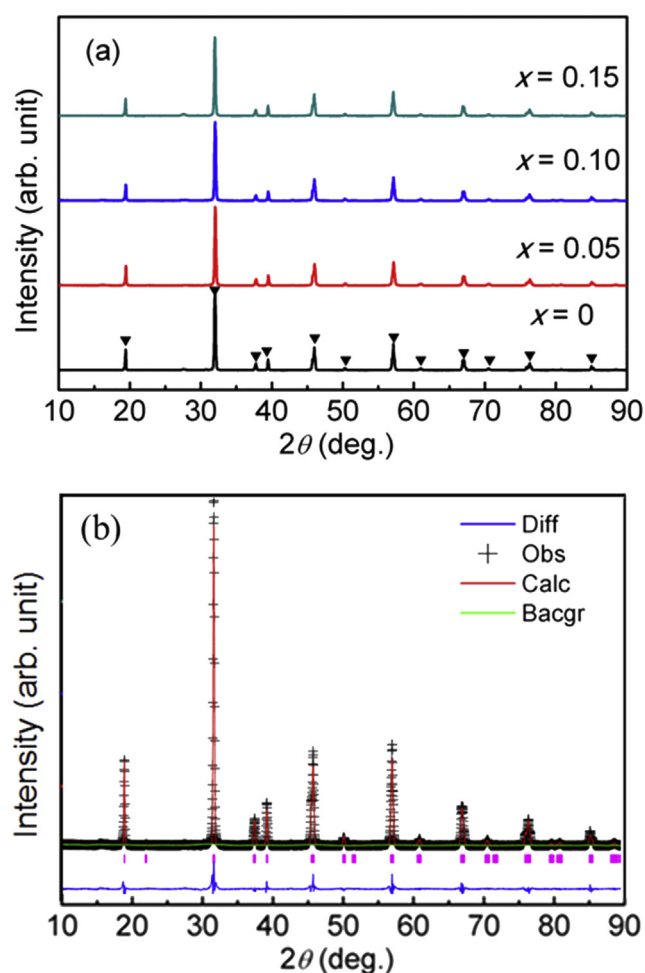**Fig. 2.** (a) XRD patterns of $Sr_{2-x}MgMoO_{6-\delta}$ samples and (b) Rietveld refinement profile for $x = 0.10$ sample obtained sintering at 1200 °C in 5% H_2/Ar atmosphere for 48 h.

Table 2
Summary of surface composition from XPS, conductivity and activation energy ($500-850\ °C$) for $Sr_{2-x}MgMoO_{6-\delta}$ ($x = 0-0.15$) samples.

x value	O_L/O_H	$[Mo^{6+}]/\Sigma[Mo]^a$	E_a(eV)	σ (S cm^{-1})
0	1.49	0.86	0.204(4)	2.4
0.05	6.35	0.88	0.162(3)	4.1
0.10	10.84	0.94	0.106(6)	15.7
0.15	5.82	0.91	0.125(5)	7.9

^{a} $[Mo^{6+}]/\Sigma[Mo]$: the molar ratio of Mo^{6+} to total amount of the metallic composition [Mo^{6+} and Mo^{5+}] on the surface.

vacancies under reducing condition, which is beneficial to the electrochemical performance.

Fig. 3b displays the Mo 3d core-level spectra of $Sr_{2-x}MgMoO_{6-\delta}$ ($x = 0-0.15$) at room temperature. High-resolution Mo 3d spectra show doublet peaks (Mo $3d_{5/2}$ and Mo $3d_{3/2}$). Curve fitting indicates that all the samples have the same peaks at 232.3 and 235.5 eV, corresponding to Mo^{6+}. For $x = 0$, $Sr_2MgMoO_{6-\delta}$ mostly contains Mo^{6+} ions, while a small amount of Mo^{5+} ions exist, which can be

confirmed by the appearance of doublet peaks at 230.5 and 234.6 eV. As x increases, the peak at 230.5 eV keeps unchanged, while the peak at 234.6 eV almost disappears when $x > 0.05$, which means that the molar ratio of Mo^{5+} decreases. We can see from Table 2 that the molar ratio of Mo^{6+} first increases and then decreases with increasing Sr-deficiency. This result is consistent well with the variation of lattice oxygen, indicating that the higher Mo valence state needs more lattice oxygen matched to keep charge neutrality. Karppinen et al. reported that the larger the difference between the charges of two B-site cations, the higher the equilibrium degree of order at B site is [26,27]. The sample with $x = 0.10$ shows the highest ξ value, indicating that the difference between Mg valence and Mo valence at B-site is the largest. Further analysis of the Mo^{6+} content for each sample was carried out by XAS analysis, as discussed latter.

It should be noticed that the variation of oxidation state of Mo determined from XPS is related to the surface information. To further confirm the Mo cation valence, the Mo L_3-edge XAS measurement was performed. In Fig. 4a, the L_3-edge features of the octahedrally coordinated compounds $Sr_{2-x}MgMoO_{6-\delta}$ ($x = 0-0.15$) are shown in comparison with the standard spectra of Sr_4Fe_3-MoO_{12}. It has been reported that by XAS investigation on Sr_2MMoO_6 (M = Co, Ni) double perovskites, the values of the Mo valence are nearly the same as that for MoO_3 and Co/Ni mostly in the divalent state [13]. The double-peak features A and B in Fig. 4a are seen in all samples spectra and can be attributed to the
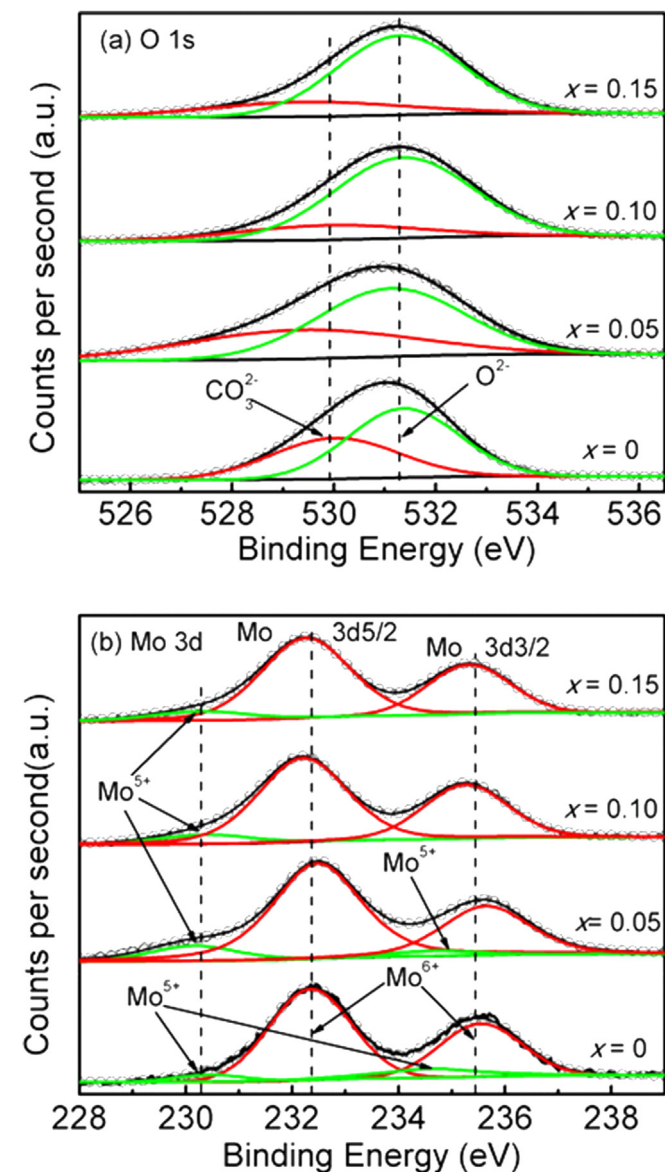

Fig. 3. Core-level spectra of double-perovskite $Sr_{2-x}MgMoO_{6-\delta}$ ($x = 0-0.15$) samples at room temperature: (a) O 1s and (b) Mo 3d.
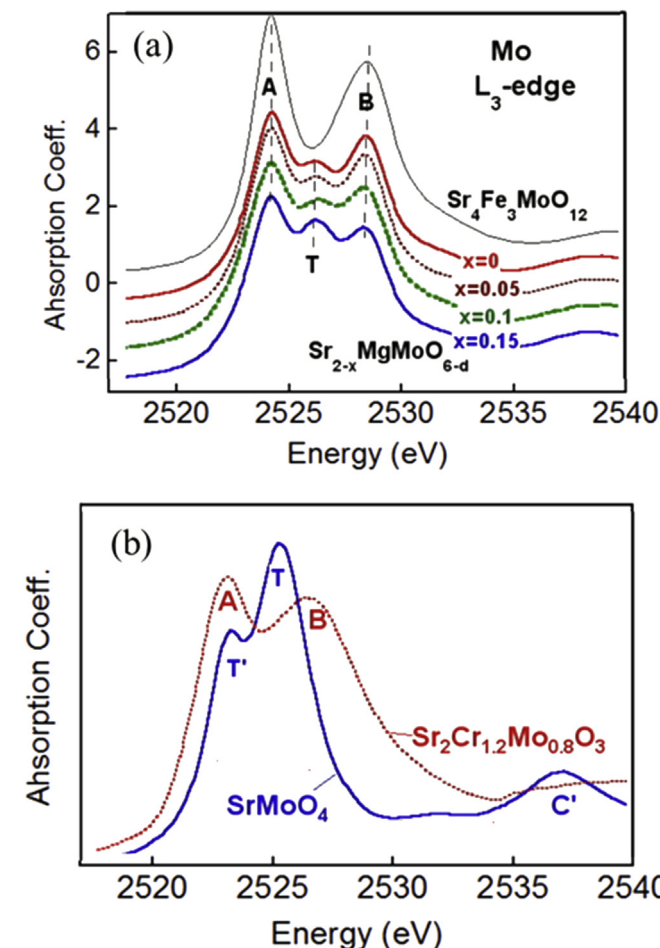
Fig. 4. Mo L_3-edge spectra for $Sr_{2-x}MgMo_{6-\delta}$ samples and standards: (a) $Sr_4Fe_3MoO_{12}$, and (b) $Sr_2Cr_{1.2}Mo_{0.8}O_3$.

2p → 4d(t_{2g}) and 2p → 4d(e_g) transitions, respectively. It can be seen that the values of edge energy (defined as the energy at inflection point of the rising part of the edge) for these four spectra are almost identical (2523.1 eV), which is relative to the lower energy Mo^{5+} peak. The noticeably feature T appearing between A and B is a signature of the existence of 4d holes in the ground states [28]. With the increasing x, the values of the edge energy increase from 2526.2 eV ($x = 0$) to 2526.6 eV ($x = 0.10$) and then decrease to 2526.4 eV ($x = 0.15$). Fig. 4b shows the standards spectra of $Sr_2Cr_{1.2}Mo_{0.8}O_3$ and $SrMoO_4$ for comparison. The higher edge energy corresponds to the higher Mo valence. The edge energy shifts to right (higher edge energy), indicating the valence of Mo closed to +6, which is consistent with the XPS result.

The oxygen vacancy plays an important role in conduction mechanism. In reducing atmosphere, the expulsion of the lattice oxygen and the formation of oxygen vacancies in $Sr_{2-x}MgMoO_{6-\delta}$ are based on the following relation [25]:

$$O_O^x + 2Mo_{Mo}^x \rightarrow V_O^{\cdot\cdot} + 2Mo_{Mo}' + \frac{1}{2}O_2\,(g) \quad (1)$$
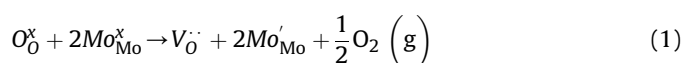
As temperature increases, the lattice oxygen O_O^x may loss, resulting in the formation of oxygen vacancies $V_O^{\cdot\cdot}$ in the lattice and partial reduction of Mo^{6+} (Mo_{Mo}^x) to Mo^{5+}(Mo_{Mo}') ions, and hence generating electronic charge carriers.

Fig. 5 presents the Arrhenius plot of electrical conductivity σ of $Sr_{2-x}MgMoO_{6-\delta}$ in pure H_2 after reduction in 5% H_2/Ar at 800 °C for 20 h. For all the samples, σ increases with temperature, which can be ascribed to the increased oxygen vacancies and Mo^{6+}/Mo^{5+} redox couple. Moritomo et al. [29] reported that the Mo–O bond length d_{Mo-O} plays a key role in perovskite structure; deceasing d_{Mo-O} may enhance hybridization between Mo 4d and O 2p orbitals. In $Sr_{2-x}MgMoO_{6-\delta}$, increasing Sr-deficiency leads to tilting of MgO_6 and MoO_6 octahedra, which consequently results in decrease of d_{Mo-O} and significant enhancement of conductivity. The electrical conductivity strongly depends on x. σ is 15.7 S cm^{-1} at 800 °C in H_2 for $x = 0.10$. With further increasing x when $x > 0.10$, the value of σ decreases, which is due to the decrease of B-site cationic ordering degree. In $Sr_{2-x}MgMoO_{6-\delta}$ family, the samples exhibit polaronic conductivity. The oxygen vacancy concentration and activation energy can be used to descript the ionic conductivity. The temperature dependence of conductivity can be described by a small-polaron hopping mechanism [12]:
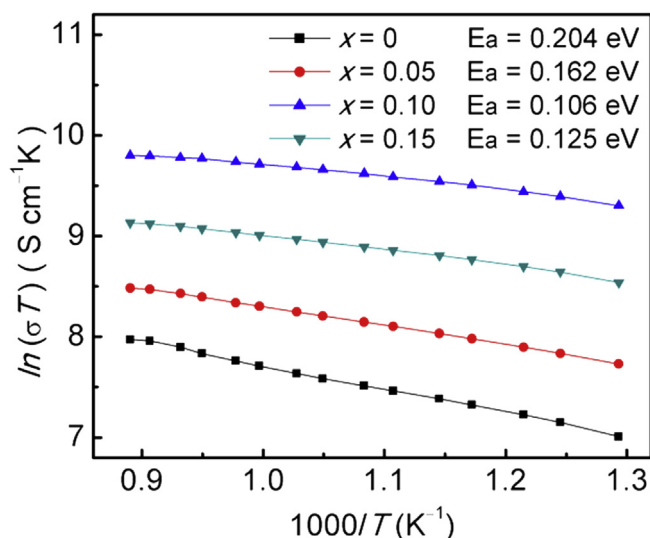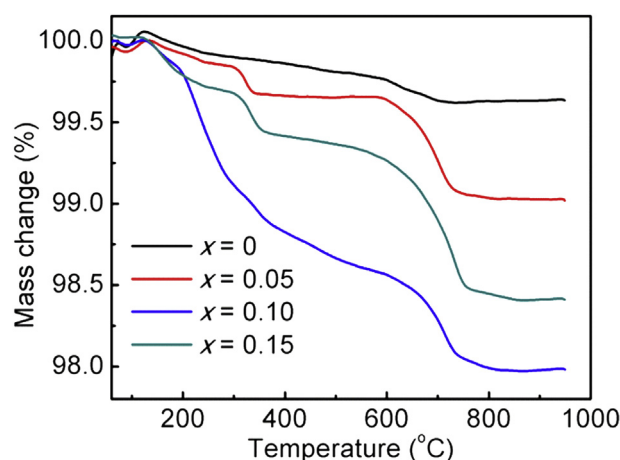

Fig. 6. TGA curves of $Sr_{2-x}MgMoO_{6-\delta}$ double-perovskite between 40 and 950 °C in 5% H_2/Ar atmosphere.

$$\sigma = \frac{A}{T}\exp\left(-\frac{E_a}{kT}\right) \quad (2)$$

where E_a represents the activation energy, A is a constant relating to the lattice structure, and k is the Boltzmann constant. The value of activated energy E_a can be obtained from the slopes of the Arrhenius plots of $\ln(\sigma T)$ vs T^{-1} that are almost lines in the interval 500 – 850 °C (see Fig. 5). The calculated E_a values are listed in Table 2. We can see that E_a gradually decreases with increasing Sr deficiency from $x = 0$ to 0.10, and reaches the minimum of 0.106 eV at $x = 0.10$. With increasing x, as described in Eq. (1), the reduction of Mo^{6+} to Mo^{5+} results in the increase of oxygen vacancy concentration and decrease of activation energy.

Eq. (1) also demonstrates that the weight of the sample may change during the formation of oxygen vacancies at elevating temperature. Marrero-López and Bernuy-Lopez et al. reported that a number of oxygen vacancies and some low-valence Mo ions could appear during reducing $Sr_2MgMoO_{6-\delta}$ [30,31]. For anode materials, oxygen vacancies are crucial to transfer of oxygen ions come from the electrolyte, while the mixed Mo^{6+}/Mo^{5+} redox couple gives rise to polaronic conduction to allow transfer of electrons [11]. Hence, TG measurement was carried out between room temperature and 950 °C under 5% H_2/Ar atmosphere. Fig. 6 shows TG curves for $Sr_{2-x}MgMoO_{6-\delta}$ ($x = 0–0.15$) samples. There are two obvious

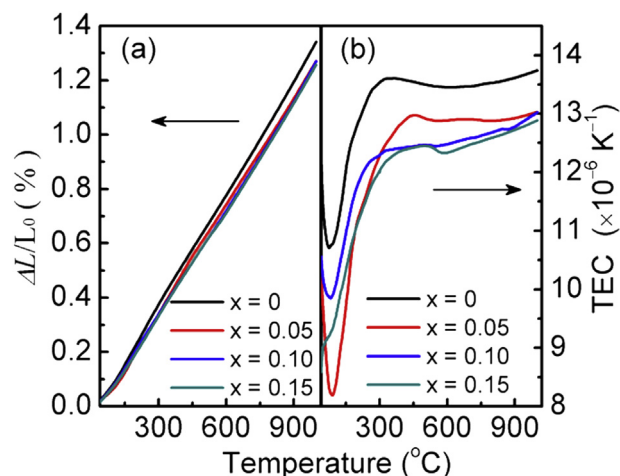**Fig. 5.** Arrhenius plots of ln (σT) vs T^{-1} for $Sr_{2-x}MgMoO_{6-\delta}$ ($x = 0–0.15$).

Fig. 7. Thermal expansion behavior of $Sr_{2-x}MgMoO_{6-\delta}$ samples between 40 and 950 °C.

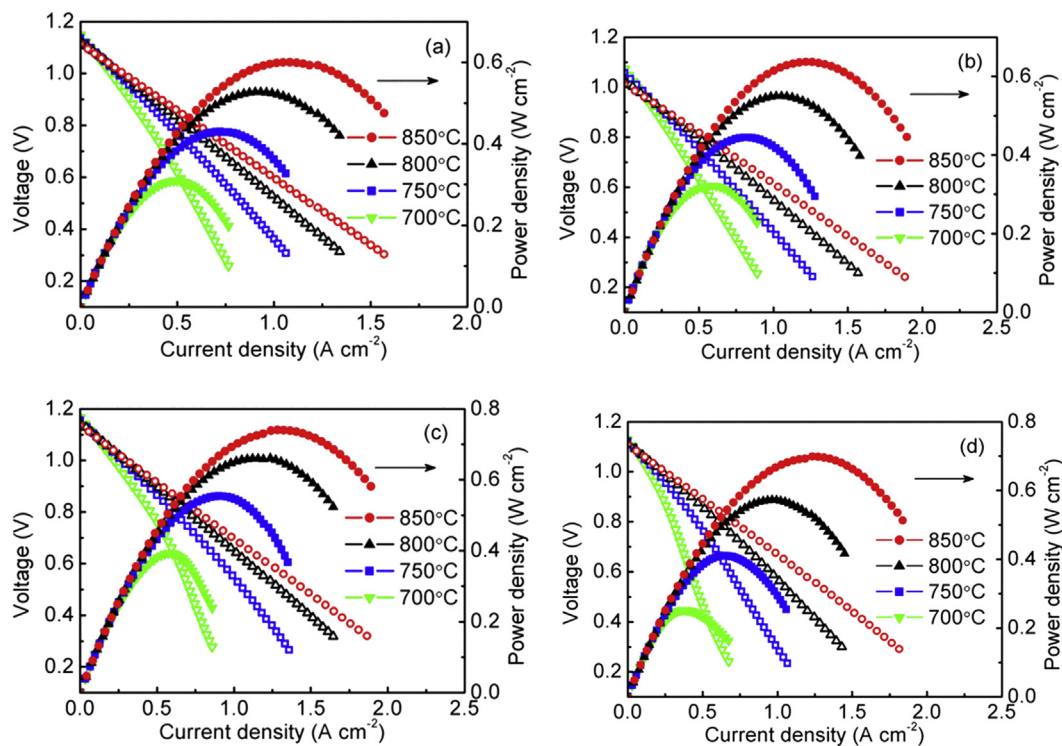**Fig. 8.** Cell voltage and power density of $Sr_{2-x}MgMoO_{6-\delta}$|SDC|LSGM|BSCF cells measured between 700 and 850 °C: (a) $x = 0$, (b) $x = 0.05$, (c) $x = 0.10$, (d) $x = 0.15$.

weight losses at around 300 and 700 °C. The first loss at around 300 °C can be ascribed to the loss of lattice oxygen due to the reducing atmosphere. The second loss at around 700 °C can be attributed to further formation of oxygen vacancies accompanied with reduction of Mo^{6+} to Mo^{5+}, which agrees well with that the weight loss caused by reduction of Mo^{6+} to Mo^{5+} can only happen at temperatures higher than 500 °C [32]. The final weight percentages at 900 °C compared to the original weight are 99.63, 99.03, 97.98 and 98.41% for $x = 0$, 0.05, 0.10 and 0.15, respectively, indicating that the yielded oxygen vacancies δ for the samples in reduction atmosphere are 0.09, 0.18, 0.38 and 0.23. The $x = 0.10$ sample produces the highest oxygen vacancy among the four samples. This result is consistent with the previous electrical conductivity analysis.

In order to judge the mechanical compatibility of the $Sr_{2-x}MgMoO_{6-\delta}$ anodes with the other components in the cell, thermal expansion measurement was carried out in a 5% H_2/Ar atmosphere. Fig. 7a shows thermal expansion behavior and Fig. 7b shows thermal expansion coefficient (TEC) for $Sr_{2-x}MgMoO_{6-\delta}$ over the temperature range of 40—950 °C. The thermal-expansion curves are almost linear and no abrupt changes occur in the TEC curves, suggesting that there is no structural transition within the measured temperature range. The mean TEC values for $x = 0$, 0.05, 0.10 and 0.15 are 13.2×10^{-6}, 12.2×10^{-6}, 12.1×10^{-6} and 11.9×10^{-6} K^{-1}, respectively, which are quite close to those of SDC interlayer (12.3×10^{-6} K^{-1}) [33] and LSGM electrolyte (11.4×10^{-6} K^{-1}) [34] under the same condition. The similar TEC values indicate that the $Sr_{2-x}MgMoO_{6-\delta}$ anodes have a good thermal expansion compatibility with SDC and LSGM under operational conditions. Moreover, the TEC value only changes within a narrow range ($11.9-13.2 \times 10^{-6}$ K^{-1}) with increasing x, which is favorable to make the SOFC stable during operation.

Fig. 8 depicts cell voltage and power density as a function of current density at different temperatures for single fuel cells with $Sr_{2-x}MgMoO_{6-\delta}$ ($x = 0-0.15$) as anodes. The open circuit voltages

(OCVs) of the cells are 1.10 V at 800 °C, close to the value predicted by the Nernst equation. At 800 °C, the maximum power density of the single cell reaches to 527, 551, 659 and 573 mW cm^{-2} corresponding to the double perovskite $Sr_{2-x}MgMoO_{6-\delta}$ anode for $x = 0$, 0.05, 0.10 and 0.15, respectively. All the single cells with $Sr_{2-x}MgMoO_{6-\delta}$ as anodes show acceptable power outputs, indicating that $Sr_{2-x}MgMoO_{6-\delta}$ anodes own good electro-catalytic performance. The values of power densities for $Sr_{2-x}MgMoO_{6-\delta}$ agree well with the order of their electrical conductivities, demonstrating that increasing electrical conductivity is helpful to improve the anode performance.

The overpotentials of $Sr_{2-x}MgMoO_{6-\delta}$ anodes and BSCF cathode measured at 800 °C are shown in Fig. 9. The dependence of overpotential on current density is almost linear. The $Sr_{2-x}MgMoO_{6-\delta}$
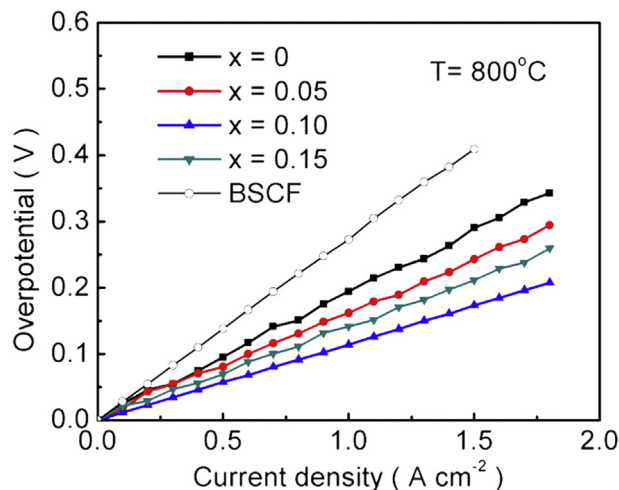

Fig. 9. The anodic and cathodic overpotentials of various electrode materials were measured at 800 °C.

anodic overpotential value is lower than that of BSCF cathode, demonstrating that the catalytic reactivity of hydrogen oxidation at the anode side is higher than that of oxygen reduction at the cathode side. With increasing x, the overpotential of the anode decreases, reaches the lowest at $x = 0.10$, and then increases when $x > 0.10$. This indicates that an appropriate Sr-deficiency in $Sr_{2-x}MgMoO_{6-\delta}$ can facilitate oxygen exchange, oxide-ion transport and charge transfer, leading to improved electrochemical performance. For instance, the overpotentials are 0.19, 0.16, 0.11 and 0.14 V under 1 A cm^{-2} at 800 °C for $x = 0$, 0.05, 0.10 and 0.15, respectively. The $Sr_{1.9}MgMoO_{6-\delta}$ anode exhibits the lowest

overpotential. Such good performance of $Sr_{1.9}MgMoO_{6-\delta}$ is mainly based on the large mount oxygen vacancies than other samples. The inspector of the anode overpotential also verifies that the $Sr_{1.9}MgMoO_{6-\delta}$ anode exhibits the highest power density of these samples.

The SEM images of cross-view and surface-view for $Sr_{2-x}MgMoO_{6-\delta}$ anodes are shown in Fig. 10. From Fig. 10a—d we can see that the electrolyte is highly dense except a very few pin-holes, and no delamination of the interlayer from the electrolyte is observed in the SEM micrographs. The anode and the interlayer keep good binding and continuous connection at the anode/
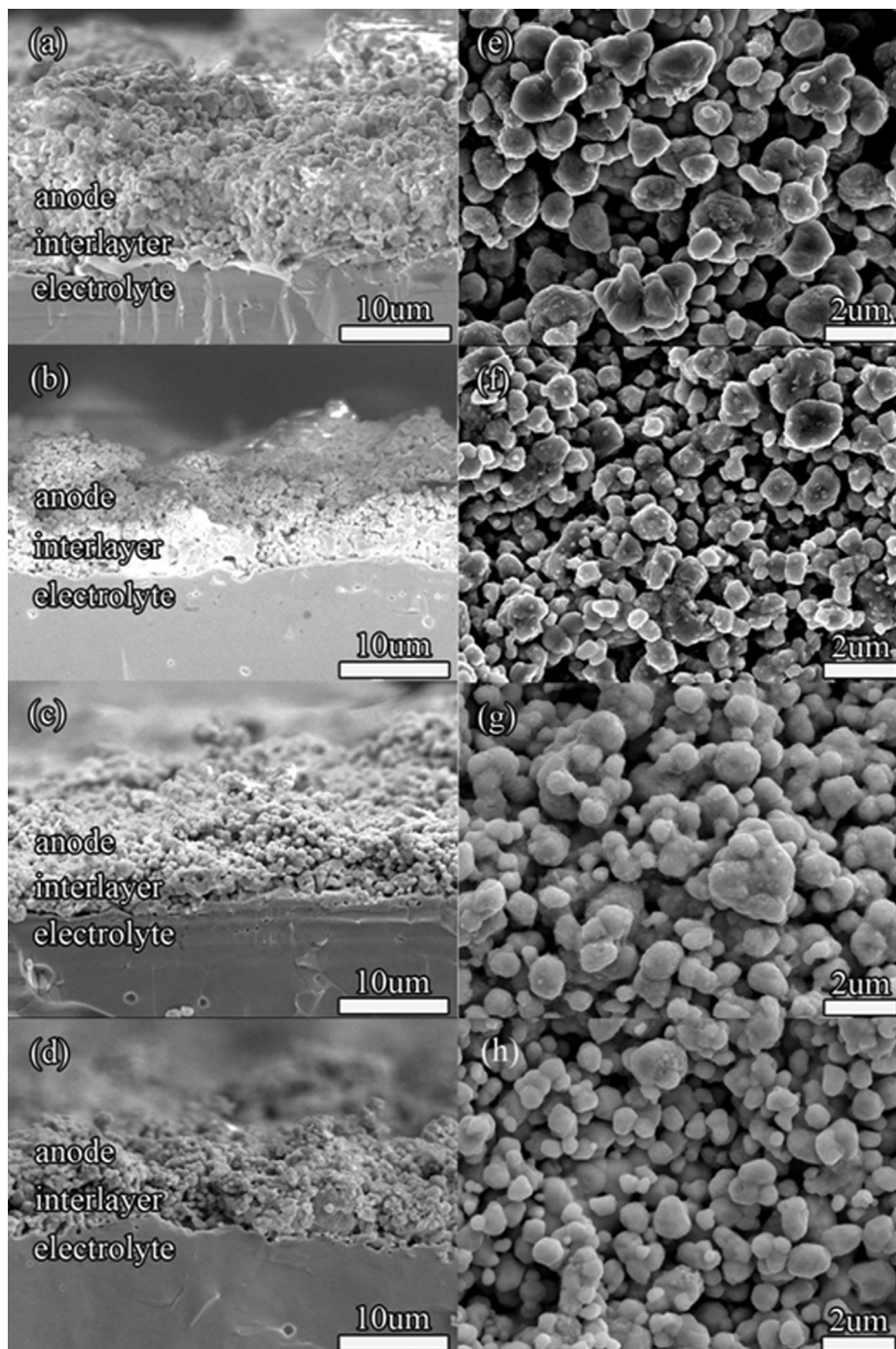

Fig. 10. SEM images for the $Sr_{2-x}MgMoO_{6-\delta}$ ($x = 0$—0.15) anodes: (a—d) cross-section, (e, f) surface-section.

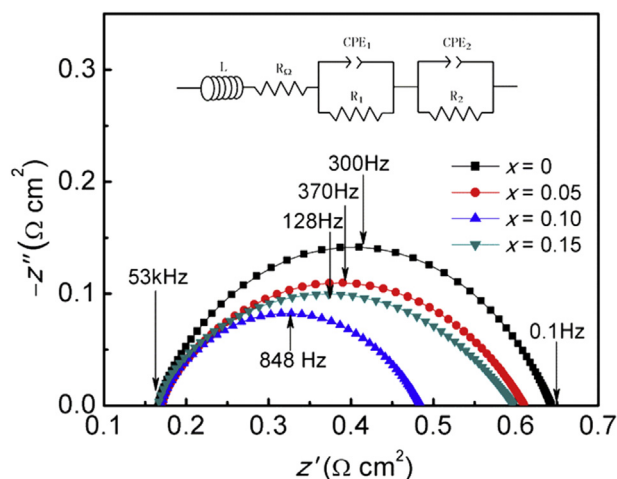**Fig. 11.** Impedance spectra for the $Sr_{2-x}MgMoO_{6-\delta}$ anodes at 800 °C.

interlayer interface, indicative of the good thermal-expansion compatibility between anode and interlayer. This can match well with the TEC data. In Fig. 10e–h, the uniform distribution of the $Sr_{2-x}MgMoO_{6-\delta}$ anodes can be observed and the mean particle size is less than 2 μm. As x increases from 0 to 0.10, the size distribution of particles becomes more and more uniform, leading to a high porosity. Good adhesion between the particles is observed in the $x = 0.10$ sample. Furthermore, inter-particle contacts in Fig. 10g ($x = 0.1$) appear to better than other samples. This will tend to increase the electrical conductivity and lower the polarization resistance. Good adhesion and uniform distribution provide the sufficient three phase boundaries for oxygen vacancies and charge, which is helpful for the cell to deliver high power output.

In order to compare the area-specific resistance (ASR) of the anode samples, the resistance spectra of the cathode and the electrolyte are subtracted from the Nyquist plot of the single cell. The spectra were analyzed with equivalent circuits to obtain the overall resistance at 800 °C. The equivalent circuit used in the fitting is schematically shown in the inset of Fig. 11. In the fitting model, L represents the inductance of the equipment. R_Ω is a serial resistance including all ohmic resistances of the cell. A constant phase element (CPE) in parallel with a resistance (R) represents the distributed element. The ASR values at 800 °C for $x = 0$, 0.05, 0.10 and 0.15 are 0.48, 0.44, 0.32 and 0.43 Ω cm^2, respectively. The $x = 0.10$ sample exhibits the lowest ASR value, which is probably related with the concentration of oxygen vacancy. Increasing oxygen vacancy is helpful to enhance catalytic activity. It should be noted that the ASR value for the $x = 0.10$ anode is consistent with that reported for symmetrical cell SMMO|CGO|LSGM|CGO|SMMO operating at 800 °C in humidified H$_2$ [25]. For the $x = 0.10$ anode, the higher electrical conductivity, lower ASR and lower overpotential are responsible for the superior cell performance.

4. Conclusions

Double-perovskite oxides of composition $Sr_{2-x}MgMoO_{6-\delta}$ have been prepared by sol–gel technique and evaluated as potential anode materials for SOFCs. The $Sr_{2-x}MgMoO_{6-\delta}$ show stable structure under reducing atmosphere. XPS and XAS analysis show that the increase of Mo^{6+} fraction enhances the oxygen vacancies. The deficiency in Sr-site can adjust the TEC value. The electrical conductivity is remarkably enhanced with deficiency at Sr-site

especially for $x = 0.10$. Single-cell testing indicates that the maximum power densities for the $Sr_{2-x}MgMoO_{6-\delta}$ electrodes are 527, 551, 659 and 573 mW cm^{-2}, respectively, for $x = 0$, 0.05, 0.10 and 0.15 at 800 °C with 280 μm-thick LSGM as electrolyte. The $x = 0.10$ sample shows particularly favorable effects of stable structure, high electrical conductivity, good thermal compatibility, and excellent electrochemical performance. Our work indicates that Sr-deficient double-perovskites are potential anode materials for high-performance SOFCs.

References

[1] B.C.H. Steele, A. Heinzel, Nature 414 (2001) 345–352.
[2] S. Tao, J.T. Irvine, Nat. Mater. 2 (2003) 320–323.
[3] A. Atkinson, S. Barnett, J.T.S. Irvine, Nat. Mater. 3 (2004) 17–27.
[4] J.B. Goodenough, Y.-H. Huang, J. Power Sources 173 (2007) 1–10.
[5] S. Tao, J.T.S. Irvine, J.A. Kilner, Adv. Mater. 17 (2005) 1734–1737.
[6] S. Lee, G. Kim, J.M. Vohs, R.J. Gorte, J. Electrochem. Soc. 155 (2008) B1179–B1183.
[7] G. Kim, M.D. Gross, W. Wang, J.M. Vohs, R.J. Gorte, J. Electrochem. Soc. 155 (2008) B360–B366.
[8] S. McIntosh, J.M. Vohs, R.J. Gorte, J. Electrochem. Soc. 150 (2003) A1305–A1312.
[9] S. Zha, P. Tsang, Z. Cheng, M. Liu, J. Solid State Chem. 178 (2005) 1844–1850.
[10] J.M. Haag, S.A. Barnett, J.W. Richardson, K.R. Poeppelmeier, Chem. Mater. 22 (2010) 3283–3289.
[11] Y.H. Huang, R.I. Dass, Z.L. Xing, J.B. Goodenough, Science 312 (2006) 254–257.
[12] Y.H. Huang, R.I. Dass, J.C. Denyszyn, J.B. Goodenough, J. Electrochem. Soc. 153 (2006) A1266–A1272.
[13] Y.-H. Huang, G. Liang, M. Croft, M. Lehtimäki, M. Karppinen, J.B. Goodenough, Chem. Mater. 21 (2009) 2319–2326.
[14] L. Zhang, Q. Zhou, Q. He, T. He, J. Power Sources 195 (2010) 6356–6366.
[15] P. Zhang, Y.-H. Huang, J.-G. Cheng, Z.-Q. Mao, J.B. Goodenough, J. Power Sources 196 (2011) 1738–1743.
[16] T. Wei, Y. Ji, X. Meng, Y. Zhang, Electrochem. Commun. 10 (2008) 1369–1372.
[17] Q. Zhang, T. Wei, Y.-H. Huang, J. Power Sources 198 (2012) 59–65.
[18] Y. Ji, Y.-H. Huang, J.-R. Ying, J.B. Goodenough, Electrochem. Commun. 9 (2007) 1881–1885.
[19] L. Zhang, T. He, J. Power Sources 196 (2011) 8352–8359.
[20] Z. Xie, H. Zhao, T. Chen, X. Zhou, Z. Du, Int. J. Hydrogen Energy 36 (2011) 7257–7264.
[21] S. Vasala, M. Lehtimäki, S.C. Haw, J.M. Chen, R.S. Liu, H. Yamauchi, M. Karppinen, Solid State Ionics 181 (2010) 754–759.
[22] L. Jiang, T. Wei, R. Zeng, W.-X. Zhang, Y.-H. Huang, J. Power Sources 232 (2013) 279–285.
[23] Z. Shao, S.M. Haile, Nature 431 (2004) 170–173.
[24] J.L.G. Fierro, Catal. Today 8 (1990) 153–174.
[25] D. Marrero-López, J. Peña-Martínez, J.C. Ruiz-Morales, M. Gabás, P. Núñez, M.A.G. Aranda, J.R. Ramos-Barrado, Solid State Ionics 180 (2010) 1672–1682.
[26] M. Karppinen, H. Yamauchi, Y. Yasukawa, J. Linden, T.S. Chan, R.S. Liu, J.M. Chen, Chem. Mater. 15 (2003) 4118–4121.
[27] S. Vasala, M. Lehtimäki, Y.H. Huang, H. Yamauchi, J.B. Goodenough, M. Karppinen, J. Solid State Chem. 183 (2010) 1007–1012.
[28] G. Liang, Q. Yao, S. Zhou, D. Katz, Phys. C Supercond. 424 (2005) 107–115.
[29] Y. Moritomo, S. Xu, A. Machida, T. Akimoto, Phys. Rev. B 61 (2000) R7827–R7830.
[30] D. Marrero-López, J. Peña-Martínez, J.C. Ruiz-Morales, D. Pérez-Coll, M.A.G. Aranda, P. Núñez, Mater. Res. Bull. 43 (2008) 2441–2450.
[31] C. Bernuy-Lopez, M. Allix, C.A. Bridges, J.B. Claridge, M.J. Rosseinsky, Chem. Mater. 19 (2007) 1035–1043.
[32] D. Logvinovich, M.H. Aguirre, J. Hejtmanek, R. Aguiar, S.G. Ebbinghaus, A. Reller, A. Weidenkaff, J. Solid State Chem. 181 (2008) 2243–2249.
[33] D. Chen, R. Ran, Z. Shao, J. Power Sources 195 (2010) 7187–7195.
[34] F. Tietz, Ionics 5 (1999) 129–139.